

A sea of tides: star formation and the central-satellite dichotomy in a continuum of tidal environments

Jolanta Zjupa^{1*}, Aseem Paranjape², Oliver Hahn¹, Rüdiger Pakmor³

¹ *Laboratoire Lagrange, Université Côte d’Azur, Observatoire de la Côte d’Azur, CNRS, Blvd de l’Observatoire, CS 34229, 06304 Nice cedex 4, France*

² *Inter-University Centre for Astronomy & Astrophysics, Ganeshkhind, Post Bag 4, Pune 411007, India*

³ *Max-Planck-Institut für Astrophysik, Karl-Schwarzschild-Str. 1, D-85748, Garching, Germany*

draft

ABSTRACT

The environment-dependent bimodality of the distribution of stellar mass (M_*) and specific star formation rate (sSFR) of galaxies, and its explanation in terms of the central-satellite dichotomy, form a cornerstone of our current understanding of galaxy evolution in the hierarchical structure formation paradigm. We revisit this framework in the IllustrisTNG simulation in the context of the *most extreme* local tidal anisotropy α_{peak} experienced by each galaxy over cosmic time, which is an excellent proxy for environmental influence. We show that, while sharing a common monotonic M_* - v_{peak} relation, central, satellite and ‘splashback’ galaxies define a *hierarchy of increasing* α_{peak} . We also find that the sSFR of objects in small haloes unaffected by feedback from an active nucleus typically decreases with increasing α_{peak} . Our results support an alternate viewpoint in which a galaxy can be identified by the value of α_{peak} ; i.e., rather than being placed on the central-satellite dichotomy, a galaxy is better classified by its location in a continuum of tidal environments. This conceptual shift can potentially yield a more robust understanding of galaxy evolution and the galaxy-dark matter connection, e.g., in accurately modelling subtle effects such as sSFR-induced secondary clustering.

Key words: cosmology: theory – galaxies: formation – methods: numerical.

1 INTRODUCTION

The persistent bimodality of the galaxy population in the plane of stellar mass (M_*) and specific star formation rate (sSFR = SFR/ M_*) and its dependence on the cosmic environment as revealed by large-volume surveys (e.g., Baldry et al. 2004; Kauffmann et al. 2004; Zehavi et al. 2011), have played a fundamental role in shaping our current understanding of galaxy formation and evolution. Observed galaxies primarily segregate into relatively weakly clustered star forming objects and strongly clustered ‘quenched’ objects. The origin of these trends, and their connection to the cosmic web, has been a subject of intense research (e.g., Dressler 1980; Weinmann et al. 2006; Peng et al. 2012; Woo et al. 2017; Poudel et al. 2017).

Explanations of this bimodality typically invoke the *central-satellite dichotomy*. In this framework (see, e.g., Skibba & Sheth 2009, and references therein), a ‘central’ galaxy forms and resides close to the gravitational centre of an independent host dark matter halo (White & Rees 1978), with its star formation regulated by feedback from supernovae or an active galactic nucleus (AGN) depending

on its mass (Dekel & Birnboim 2006). On the other hand, a ‘satellite’ resides in a subhalo of a larger host, having been a central before the merger event that transformed its own host into a subhalo. The (typically crowded and hot) environment of the group host leads to additional satellite-specific processes such as strangulation, ram pressure stripping, and others, which effectively decrease the amount of fuel available for star formation (see, e.g., van den Bosch et al. 2008, and references therein). Star formation activity thus strongly correlates with galaxy type and hence environment: low-mass star forming objects are predominantly centrals and hence relatively weakly clustered compared to quenched objects of similar M_* which are predominantly satellites of more massive (and typically AGN-quenched) centrals.

Implementations of these ideas using empirical techniques lead to excellent descriptions of the dependence of galaxy clustering on sSFR and M_* (equivalently, colour and luminosity) (Skibba & Sheth 2009; Zehavi et al. 2011). M_* -dependent clustering, in particular, is succinctly captured by subhalo abundance matching (SHAM) of M_* and v_{peak} , the largest value of the galaxy’s maximum circular velocity over cosmic time (Reddick et al. 2013), which is a mass proxy effectively set at the epoch of the last major merger (Behroozi et al. 2014).

* E-mail: jolanta.zjupa@oca.eu

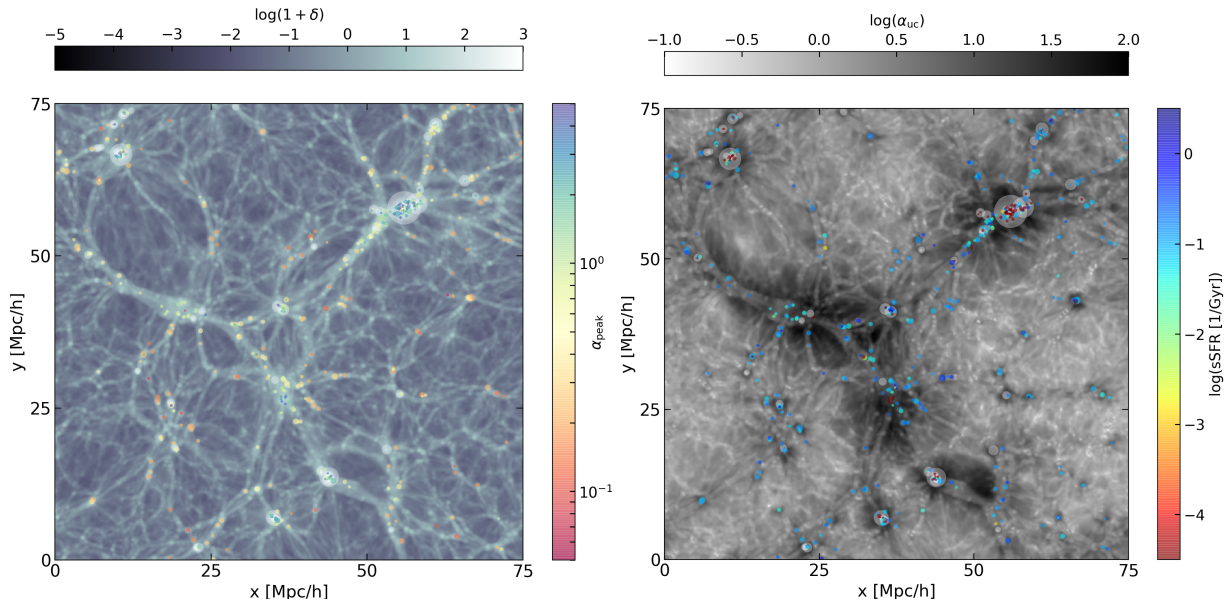


Figure 1. Single-cell ‘razor thin’ slice through the TNG100 box, showing galaxies (circles, pentagons, and diamonds for centrals, satellites, and splashbacks, respectively) on a background showing overdensity δ (left panel) and a modified tidal anisotropy $\alpha_{uc} = \alpha \times (1 + \delta)^{0.51}$ (right panel) evaluated on a 1024^3 grid with 250 kpc Gaussian smoothing. α_{uc} is defined to have zero correlation with δ (see Alam et al. 2019). We display it to illustrate the difference between density and the tidal field at a fixed small smoothing scale; the variable α is thus a non-linear, scale-dependent combination of α_{uc} and δ . Galaxies lie within 2 Mpc of the density slice with sizes scaled to $4R_{vir}$ of the host (sub)halo (the adaptive scale at which α_{peak} is extracted for each galaxy). For objects with $v_{peak} \leq 190 \text{ km s}^{-1}$, marker colours in the left (right) panel show the host-centric α_{peak} (galaxy sSFR); larger objects are transparent and white.

As regards the influence of the cosmic web, simulations indicate that cosmic filaments can channel cold gas into low-mass haloes (Kereš et al. 2005). The local tidal environment also strongly influences halo mass accretion and mass loss in the vicinity of large objects, thus potentially regulating star formation (Hahn et al. 2009; Behroozi et al. 2014). The corresponding ‘assembly bias’ imprints in galaxy clustering, however, remain observationally elusive (e.g., Alam et al. 2019). Indeed, simplified models of galaxy evolution which treat centrals and satellites separately (e.g., Davé et al. 2012; Birrer et al. 2014) provide reasonable descriptions of star formation trends with environment. A tidal influence on star formation, *having assumed the central-satellite dichotomy*, is therefore weak at best.

In this *Letter*, we present evidence for an alternate viewpoint, in which star formation activity can be tied to a *continuous measure* of the degree of environmental influence. Using the IllustrisTNG simulation, we show that the central-satellite dichotomy is, in fact, better represented as a continuum of *increasing anisotropy* of the local tidal environment of a galaxy as we progress from centrals to satellites to splashback objects.¹ Moreover, within each category, the sSFR of low-mass objects steadily decreases with increasing tidal anisotropy. Thus, the degree of tidal anisotropy acts as an excellent environmental proxy which blurs the distinction between traditional (star forming) centrals and (quenched) satellites. We describe the simulation and our analysis in section 2, present our results in section 3 and conclude with our arguments in section 4. Throughout, we refer to objects with $\text{sSFR} > 0.2 \text{ Gyr}^{-1}$ ($< 0.01 \text{ Gyr}^{-1}$) as ‘star forming’ (‘quenched’) (e.g., Genel et al. 2015).

¹ Splashbacks are current-epoch centrals that passed through a larger host in the past. We give a more detailed definition below.

2 SIMULATION & ANALYSIS

We use the outputs of the cosmological hydrodynamical simulation TNG100 from the galaxy formation simulation suite IllustrisTNG, focusing on results at $z = 0$. TNG100 evolves a $75 h^{-1} \text{ Mpc}$ periodic box using the Planck Collaboration et al. (2016) cosmology and subgrid models for galaxy formation physics including, among others, recipes for star formation, stellar feedback in the form of galactic winds, black hole formation and growth, and AGN feedback.

The subgrid models successfully reproduce the observed stellar mass function, the evolving SFR density and SFR- M_* relation, and the low- z M_* - and colour-dependent clustering (Springel et al. 2018; Pillepich et al. 2018; Nelson et al. 2018; Marinacci et al. 2018; Naiman et al. 2018). A key element for many of these successes is a new AGN feedback model in which black holes with masses $\gtrsim 2 \times 10^8 M_\odot$, found in galaxies with $M_* \gtrsim 10^{10.5} M_\odot$ ($v_{peak} \gtrsim 190 \text{ km s}^{-1}$, see below), transition from purely thermal feedback to driving kinetic winds which rapidly quench star formation (Weinberger et al. 2017, 2018).

2.1 Galaxy populations

We identify galaxies using the group finder SUBFIND (Springel et al. 2001). Applying a (conservative) ≥ 300 stellar particles cut for galaxies with well-resolved sSFR at $z = 0$ results in 17893 satellite galaxies hosted in subhaloes and 19066 ‘central’ galaxies hosted at the potential minimum of (group) hosts. For the latter, we use SUBLINK (Rodríguez-Gomez et al. 2015) ‘baryonic’ merger trees – constructed using only stellar particles and star forming gas to identify objects, which allows for robust tracking of orphan galaxies – to follow each main progenitor back in time until $z = 1$ (lookback time $\simeq 8 \text{ Gyr}$). Objects which were identified, in any snapshot

during $1 \geq z > 0$, as satellites of hosts with centrals at least 3 times more massive than the pre-merger progenitor, are then labelled splashbacks,² while the remaining objects are designated centrals.

We use v_{peak} to account for the influence of a galaxy's host (sub)halo in establishing environmental trends (see above), allowing for a simultaneous discussion of all galaxy types, by-passing the complication of tidal effects on the dark matter content of substructure (Chaves-Montero et al. 2016). For each galaxy, we use the main progenitor branch of the merger trees to extract at each epoch the maximum value v_{max} of its rotation curve, whose maximum over time yields v_{peak} . We also separately treat objects with host $R_{\text{vir}} < 60.4 \text{ kpc}$ comoving for which we do not have reliable estimates of the tidal environment (see below). Excluding these yields 17666 centrals, 9468 satellites, and 1300 splashbacks in our final sample. For each object, we use values of M_* and instantaneous sSFR in our analysis.

2.2 Local tidal environment

For a galaxy in a host with virial radius R_{vir} , we first characterise its local environment using the *tidal anisotropy* scalar α extracted from the host-centric tidal tensor Gaussian-smoothed at scale $R_h \equiv 4R_{\text{vir}}/\sqrt{5}$ (Paranjape et al. 2018). In terms of the eigenvalues $\lambda_1, \lambda_2, \lambda_3$ of the smoothed tidal tensor $\psi_{,ij} = \partial^2 \psi / \partial x^i \partial x^j$ (where the normalised gravitational potential ψ satisfies the Poisson equation $\nabla^2 \psi = \delta$), α is defined as

$$\alpha \equiv \sqrt{q^2} / (1 + \delta), \quad (1)$$

where $\delta = \lambda_1 + \lambda_2 + \lambda_3$ is the total matter overdensity and $q^2 = (1/2) [(\lambda_1 - \lambda_2)^2 + (\lambda_2 - \lambda_3)^2 + (\lambda_3 - \lambda_1)^2]$ is the tidal shear, so that $\alpha \geq 0$. Haloes in filaments have $\alpha \geq 0.5$ while subhaloes span both larger and smaller values depending on their host-centric distance (Paranjape 2020).

To determine α for each galaxy, we first calculate the overdensity field $\delta(\mathbf{x})$ in the full TNG100 volume on a 1024^3 grid using cloud-in-cell interpolation, then Fourier transform and Gaussian-smooth this on 17 (approximately logarithmically spaced) smoothing scales R_G between 108 kpc and 5 Mpc,³ to obtain the k -space fields $\delta(\mathbf{k}; R_G) = \delta(\mathbf{k}) e^{-k^2 R_G^2/2}$. The smoothed tidal tensor fields $\psi_{,ij}(\mathbf{x}; R_G)$ are obtained as the inverse Fourier transform of $(k_i k_j / k^2) \delta(\mathbf{k}; R_G)$ for each R_G . These are interpolated spatially and across smoothing scales to obtain the (sub)halo-centric $\psi_{,ij}(\mathbf{x}_h; R_h)$ at the location \mathbf{x}_h of the galaxy's host at scale R_h (see above), diagonalising which finally leads to a value of α for the galaxy using equation (1).

Ramakrishnan et al. (2019) showed that this definition of α with its choice of adaptive smoothing scale is an excellent indicator of halo assembly bias, particularly for objects whose current tidal environment is the most extreme they have experienced. This motivates us to focus on α_{peak} , the maximum of α for an object over cosmic time, as a proxy for environmental influence. We calculate the tidal tensor and (sub)halo-centric α as discussed above in each snapshot

between $1 \geq z > 0$ and extract α_{peak} for each object (similarly to v_{peak}) along with the redshift $z_{\alpha_{\text{peak}}}$ at which the maximum occurred.

Figure 1 visualises a single-cell slice through the simulation, chosen to contain a few clusters and some filaments, with galaxies shown by the markers on a background of the density δ and a modified tidal anisotropy α_{uc} in the *left* and *right panels*, respectively (see the figure caption for details).

3 RESULTS

Figure 2 shows the distribution of v_{peak} against M_* (sSFR) in the *top* (*bottom*) *panels* for centrals, satellites and splashbacks, with coloured histograms showing the median value of α_{peak} in each bin, overlaid with solid contours of equal number. For each galaxy type, in the *top panels* we see a tight correlation between M_* and v_{peak} . The dotted contours in the *top middle* and *right panels* repeat the M_* - v_{peak} relation for centrals; this is evidently identical to the relation for satellites and splashbacks.⁴ The most striking feature of the *top panels*, however, is the steady increase in typical α_{peak} values as we progress from centrals \rightarrow satellites \rightarrow splashbacks.

The *bottom panels* of Figure 2 show the bimodality of sSFR as a function of v_{peak} . Objects with sSFR = 0 in the simulation are visualised as narrow clouds near the bottom of each panel.⁵ We see the usual trend of star forming (quenched) objects being mostly centrals (satellites). Splashbacks form a small, predominantly quenched population. Additionally, the sSFR- v_{peak} distribution coloured by α_{peak} shows some remarkable features.

At $v_{\text{peak}} \gtrsim 190 \text{ km s}^{-1}$ (or $M_* \gtrsim 10^{10.5} M_\odot$ as inferred from the *top panels*), most objects are in isotropic environments ($\alpha_{\text{peak}} \lesssim 0.3$ for centrals, somewhat larger for satellites). The downturn and suppression of sSFR apparent for centrals and satellites is due to AGN activity in massive haloes (see section 2), uncorrelated with tidal environment.

At $v_{\text{peak}} \lesssim 190 \text{ km s}^{-1}$, on the other hand, AGN do not play a role in the IllustrisTNG model. Instead, the peak tidal anisotropy α_{peak} takes centre-stage:

- (i) Star forming centrals and satellites *exclusively occupy* low- α_{peak} environments.
- (ii) As we decrease the sSFR of centrals and satellites at fixed v_{peak} , α_{peak} steadily increases, ending in objects with sSFR = 0 which predominantly live in high- α_{peak} environments. Focusing on *non star forming* objects (i.e. sSFR < 0.2 Gyr⁻¹), when sSFR \neq 0 we find Spearman rank correlation coefficients between $\alpha_{\text{peak}} \leftrightarrow$ sSFR of ~ -0.1 (-0.35) for centrals (satellites), independent of v_{peak} . For objects with sSFR = 0, the median α_{peak} values are 1.75 (2.45) for centrals (satellites).

⁴ Dashed contours and transparent histograms (prominent in the middle panels) indicate objects with $R_{\text{vir}} < 60.4 \text{ kpc}$ comoving, for which we can only measure α , and hence α_{peak} , at the grid scale $R_G = 108 \text{ kpc}$ comoving. Of these, the low- α_{peak} , high-sSFR satellites (labelled ‘starburst’) scatter the most off the M_* - v_{peak} relation. These are possibly recent major mergers, which could explain why Chaves-Montero et al. (2016) found that defining v_{peak} while an object is dynamically relaxed yields the tightest correlation with M_* .

⁵ We artificially assigned a small value of sSFR to these objects by adding a Gaussian scatter of 0.2 dex around $\log(\text{sSFR}/\text{Gyr}^{-1}) = -8.5$.

² We expect $z = 1$ to be a sufficiently early epoch to identify passage through a group host. We have checked that minor variations in the mass ratio do not affect our results.

³ The smallest scale is set by the grid size and in turn sets the minimum host R_{vir} we can use.

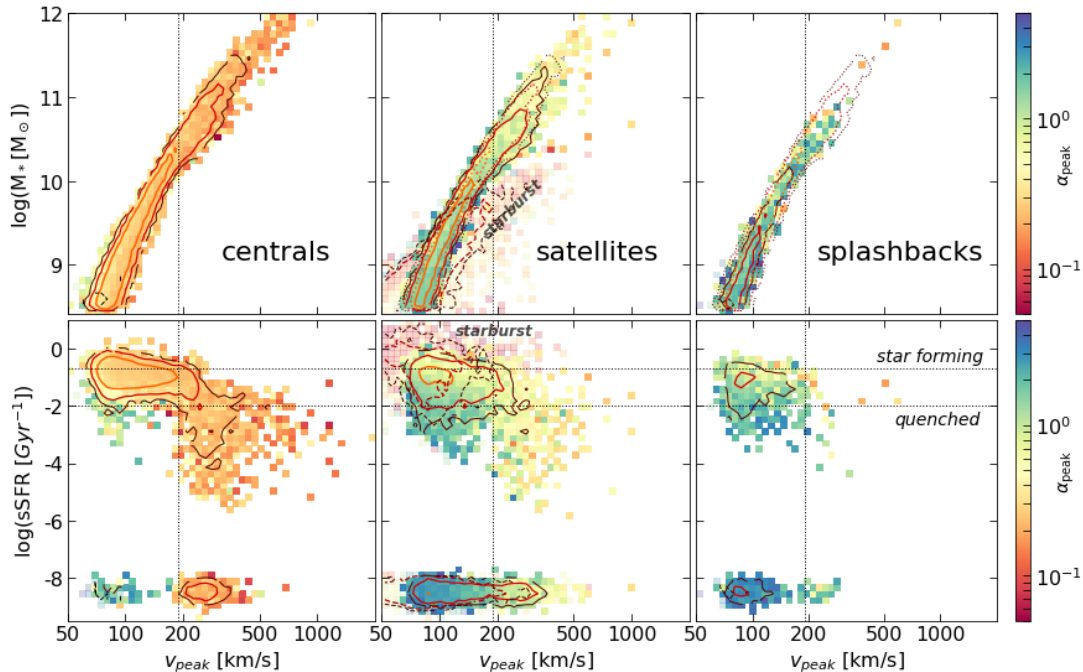


Figure 2. Distribution of v_{peak} against M_* (top panels) and sSFR (bottom panels) for central, satellite, and splashback galaxies identified in the Illustris TNG100 box (respectively, left, middle and right panels). Coloured histograms indicate the median value of peak tidal anisotropy α_{peak} , calculated for each object as in section 2.2, overlaid with solid contours of equal galaxy number (orange, red and brown for 100, 20 and 5 objects, respectively). Dotted contours in the top middle and top right panels repeat the M_* - v_{peak} contours for central galaxies from the top left panel. Dashed contours and transparent histograms indicate objects with $R_{\text{vir}} < 60.4$ kpc (see text). Clouds near $\log(\text{sSFR}/\text{Gyr}^{-1}) = -8.5$ in the bottom panels represent objects with $\text{sSFR} = 0$ in the simulation. Vertical dotted line in each panel indicates $v_{\text{peak}} = 190 \text{ km s}^{-1}$ which we use to segregate small and large objects. Horizontal dotted lines in the bottom panels indicate the thresholds used to define actively star forming and quenched galaxies.

(iii) Although splashbacks are predominantly quenched and in overall higher- α_{peak} environments, the same trends are apparent. The $\alpha_{\text{peak}} \leftrightarrow \text{sSFR}$ Spearman coefficient for *non star forming* splashbacks with $\text{sSFR} \neq 0$ is ~ -0.6 and the median α_{peak} for $\text{sSFR} = 0$ objects is 2.9. In fact, we find that the small population of $\text{sSFR} = 0$ centrals is similar to the $\text{sSFR} = 0$ splashbacks as regards the distribution of α_{peak} and hence location in the cosmic web. These objects are possibly splashbacks misclassified as centrals due to resolution limitations of the merger tree. Thus, the trend of overall α_{peak} increasing from centrals to splashbacks comes back full circle for the quenched population.

Figure 1 reflects the trends discussed above, particularly the fact that the lowest star formation is restricted to objects with the highest anisotropy. We have checked that similar trends are *not* apparent when using δ smoothed at the same adaptive scale as α (and hence α_{peak}), but do emerge for δ at much larger ($\sim 4\times$) smoothing scales, consistent with previous results on halo assembly bias (Paranjape et al. 2018).

Figure 3 shows that the quenched fraction f_q of galaxies of each type (a) increases steeply with α_{peak} and (b) has similar magnitude for all types if we exclude objects with $z_{\alpha_{\text{peak}}} < 0.15$ for which α achieved its maximum within the last 2 Gyr. We discuss these trends below.

4 DISCUSSION

The steady increase of local peak tidal anisotropy α_{peak} from centrals to satellites and from star forming to quenched objects in Figure 2 is suggestive of a continuous hierarchy of

tidal environments that spans the low-mass central-satellite dichotomy. This idea is reinforced by the fact that splashback objects (which spatially mimic centrals but are physically closer to satellites) emerge as an extreme population with high α_{peak} and low sSFR. This is also consistent with previous results showing that the tidal influence of a satellite’s group host extends well outside its R_{vir} (Behroozi et al. 2014; Diemer 2020; Bakels et al. 2020). Since the local tidal anisotropy is also known to have a strong positive correlation with large-scale clustering (Paranjape et al. 2018), the continuum of tidal anisotropy naturally accounts for the environment-dependence of the sSFR- M_* bimodality.

One might also ask whether α_{peak} can explain the bimodality itself. If so, the quenched fraction f_q of each galaxy type should be set by α_{peak} alone, with galaxies being preferentially quenched in anisotropic environments, regardless of their identity as central, satellite, or splashback. Figure 3 shows that α_{peak} is, in fact, a strong indicator of f_q for each type. When considering the full sample (thin lines), however, f_q for centrals is about a factor 5 lower than that of satellites and splashbacks. Such a deficit is not surprising, since galaxy quenching is expected to occur over timescales of $\lesssim 2$ Gyr after the event that set α_{peak} (such as accretion onto a cluster; see, e.g., Maier et al. 2019). We can allow for a delay of this magnitude by excluding objects for which $z_{\alpha_{\text{peak}}} \lesssim 0.15$. The thick lines in the figure show that applying such a cut indeed removes most of the differences between f_q for the different galaxy types, with the effect being strongest for the centrals. The excluded centrals would be predicted to quench their star formation within ~ 2 Gyr. Indeed, we find that the median gas fraction of centrals with $z_{\alpha_{\text{peak}}} \leq 0.15$ and $\alpha_{\text{peak}} > 1$ is

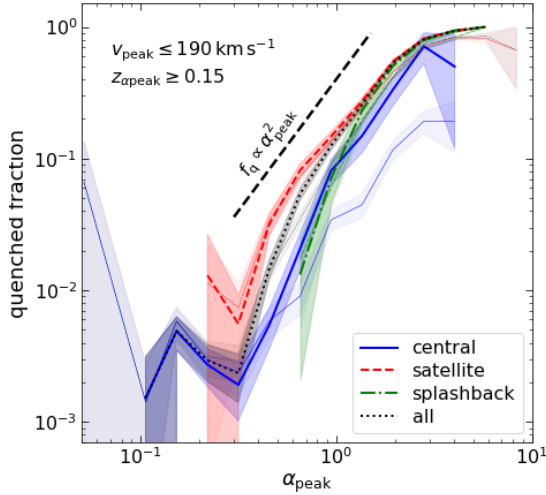


Figure 3. Quenched fraction f_q as function of α_{peak} for objects with $v_{\text{peak}} \leq 190 \text{ km s}^{-1}$. For each galaxy type, we bin objects by α_{peak} and evaluate f_q as the ratio of number of objects with $\text{sSFR} < 0.01 \text{ Gyr}^{-1}$ to the total number in each α_{peak} bin. Thin lines are for the full sample while thick lines show results when excluding objects with $z_{\alpha_{\text{peak}}} < 0.15$ (lookback time $\lesssim 2 \text{ Gyr}$). Bands show errors from 200 bootstrap samples. Black dashed line segment illustrates the behaviour $f_q \propto \alpha_{\text{peak}}^2$ for comparison.

$\sim 25\%$ smaller than of all centrals with $v_{\text{peak}} \leq 190 \text{ km s}^{-1}$, indicating the onset of gas stripping.

All of this strongly suggests that, just as v_{peak} is an excellent indicator of stellar mass regardless of galaxy type, the relevant indicator of star formation is α_{peak} . The combination of v_{peak} and α_{peak} essentially erases the dichotomy between centrals and satellites as regards star formation activity: star forming centrals on one hand and quenched satellites on the other are simply extremes in a continuum of tidal environments. SHAM with $(v_{\text{peak}}, \alpha_{\text{peak}})$ will therefore be very interesting to pursue.

We emphasize that the link between sSFR and α_{peak} is a statistical one; the physics of star formation inherently occurs at scales much smaller than $4R_{\text{vir}}$ and is likely only indirectly affected by α_{peak} . We also caution that some of our results (such as the specific value $v_{\text{peak}} \simeq 190 \text{ km s}^{-1}$ for the onset of AGN effects) could represent subgrid choices in the IllustrisTNG galaxy formation model. We expect, however, that our overall conclusions are robust to subgrid modelling, since they rely on broad properties of galaxies and the cosmic web.

The shift from a dichotomy to a continuum potentially affects the understanding of halo models as well as semi-analytical and empirical models of galaxy evolution. For example, our results open up the exciting possibility of using the $\alpha_{\text{peak}} \leftrightarrow \text{sSFR}$ connection (calibrated in small-volume galaxy formation simulations) to easily model the secondary clustering bias caused by an sSFR -dependent galaxy sample selection. More direct observational tests would require overcoming the challenges of stochastic biasing and non-linear redshift space effects when estimating the local tidal environment of galaxies. We will explore these ideas in future work.

Acknowledgments: We thank R. Srianand for useful conversations, R. Angulo for comments on an earlier draft, and V. Rodriguez-Gomez for kindly providing us the baryonic version of the SUBLINK merger trees. JZ and OH acknowledge funding from the European Research Council (ERC) under the European

Union’s Horizon 2020 research and innovation programme, Grant agreement No. 679145 (COSMO-SIMS). AP acknowledges funding from the Associateship Scheme of ICTP, Trieste and the Ramanujan Fellowship of the DST, Govt of India.

Data availability: IllustrisTNG data is publicly available at tng-project.org (Nelson et al. 2019).

REFERENCES

- Alam S., Zu Y., Peacock J. A., Mandelbaum R., 2019, *MNRAS*, **483**, 4501
- Bakels L., Ludlow A. D., Power C., 2020, arXiv e-prints, p. [arXiv:2008.05475](https://arxiv.org/abs/2008.05475)
- Baldry I. K., Glazebrook K., Brinkmann J., Ivezić Ž., Lupton R. H., Nichol R. C., Szalay A. S., 2004, *ApJ*, **600**, 681
- Behroozi P. S., Wechsler R. H., Lu Y., Hahn O., Busha M. T., Klypin A., Primack J. R., 2014, *ApJ*, **787**, 156
- Birrer S., Lilly S., Amara A., Paranjape A., Refregier A., 2014, *ApJ*, **793**, 12
- Chaves-Montero J., Angulo R. E., Schaye J., Schaller M., Crain R. A., Furlong M., Theuns T., 2016, *MNRAS*, **460**, 3100
- Davé R., Finlator K., Oppenheimer B. D., 2012, *MNRAS*, **421**, 98
- Dekel A., Birnboim Y., 2006, *MNRAS*, **368**, 2
- Diemer B., 2020, arXiv e-prints, p. [arXiv:2007.10992](https://arxiv.org/abs/2007.10992)
- Dressler A., 1980, *ApJ*, **236**, 351
- Genel S., Fall S. M., Hernquist L., Vogelsberger M., Snyder G. F., Rodriguez-Gomez V., Sijacki D., Springel V., 2015, *ApJ*, **804**, L40
- Hahn O., Porciani C., Dekel A., Carollo C. M., 2009, *MNRAS*, **398**, 1742
- Kauffmann G., White S. D. M., Heckman T. M., Ménard B., Brinchmann J., Charlot S., Tremonti C., Brinkmann J., 2004, *MNRAS*, **353**, 713
- Kereš D., Katz N., Weinberg D. H., Davé R., 2005, *MNRAS*, **363**, 2
- Maier C., Ziegler B. L., Haines C. P., Smith G. P., 2019, *A&A*, **621**, A131
- Marinacci F., et al., 2018, *MNRAS*, **480**, 5113
- Naiman J. P., et al., 2018, *MNRAS*, **477**, 1206
- Nelson D., et al., 2018, *MNRAS*, **475**, 624
- Nelson D., et al., 2019, *Computational Astrophysics and Cosmology*, **6**, 2
- Paranjape A., 2020, arXiv e-prints, p. [arXiv:2006.13954](https://arxiv.org/abs/2006.13954)
- Paranjape A., Hahn O., Sheth R. K., 2018, *MNRAS*, **476**, 3631
- Peng Y.-j., Lilly S. J., Renzini A., Carollo M., 2012, *ApJ*, **757**, 4
- Pillepich A., et al., 2018, *MNRAS*, **475**, 648
- Planck Collaboration et al., 2016, *A&A*, **594**, A1
- Poudel A., Heinämäki P., Tempel E., Einasto M., Lietzen H., Nurmi P., 2017, *A&A*, **597**, A86
- Ramakrishnan S., Paranjape A., Hahn O., Sheth R. K., 2019, *MNRAS*, **489**, 2977
- Reddick R. M., Wechsler R. H., Tinker J. L., Behroozi P. S., 2013, *ApJ*, **771**, 30
- Rodriguez-Gomez V., et al., 2015, *MNRAS*, **449**, 49
- Skibba R. A., Sheth R. K., 2009, *MNRAS*, **392**, 1080
- Springel V., White S. D. M., Tormen G., Kauffmann G., 2001, *MNRAS*, **328**, 726
- Springel V., et al., 2018, *MNRAS*, **475**, 676
- Weinberger R., et al., 2017, *MNRAS*, **465**, 3291
- Weinberger R., et al., 2018, *MNRAS*, **479**, 4056
- Weinmann S. M., van den Bosch F. C., Yang X., Mo H. J., 2006, *MNRAS*, **366**, 2
- White S. D. M., Rees M. J., 1978, *MNRAS*, **183**, 341
- Woo J., Carollo C. M., Faber S. M., Dekel A., Tacchella S., 2017, *MNRAS*, **464**, 1077
- Zehavi I., et al., 2011, *ApJ*, **736**, 59
- van den Bosch F. C., Aquino D., Yang X., Mo H. J., Pasquali A., McIntosh D. H., Weinmann S. M., Kang X., 2008, *MNRAS*, **387**, 79